Computational Condensed Matter 20 (2019) e00383

Contents lists available at ScienceDirect

Computational Condensed Matter

journal homepage: http://ees.elsevier.com/cocom/default.asp

First-principles study of structural and vibrational properties of $SrHfO_3$ compared to $SrZrO_3$

Safari Amisi

Laboratoire de Physique des Solides et des Interfaces (LPSI), Institut Supérieur Pédagogique de Bukavu, Democratic Republic of the Congo

ARTICLE INFO

Article history:
Received 26 February 2019
Received in revised form
17 March 2019
Accepted 17 March 2019

ABSTRACT

The structural and vibrational properties of $SrHfO_3$ compared to those of the $SrZrO_3$ were investigated using first-principles calculations. The phonon dispersion curves, reported in the high-symmetry cubic perovskite phase, point out the coexistence of structural antiferrodistortive instabilities at the *R* and *M* zone-boundary points and a ferroelectric instability at the zone center. Different possible intermediate phases are characterized by comparing their internal energies, giving the same hierarchy of phases as for the $SrZrO_3$. The main features of the ferroelectric instability are also discussed, and, contrary to what was found for $SrZrO_3$, it seems very unlikely to induce the ferroelectricity in the $SrHfO_3$ *Pnma* ground state either by compressive or tensile epitaxial strain.

1. Introduction

The oxide perovskites compounds (ABO_3) exhibit a variety of interesting physical properties, which can be exploited in a wide range of applications such as optoelectronic, spintronic, thermoelectric, high-dielectric, ferroelectric/piezoelectric and multiferroic materials [1]. Among them, strontium hafnium oxide ($SrHfO_3$) is a most promising candidate due to their large dielectric constant and sufficient band offsets for electrons and holes which can be use as a high-*k* gate dielectric material for use in memories, capacitors, complementary metal-oxide-semiconductor (CMOS) and metal-oxide semiconductor field-effect transistor (MOSFET) technology [2–4]. Subject of several experimental [2–8] and theoretical [9–15] studies, various structural phase transitions are reported in this compound (Table 1).

Since $SrHfO_3$ is supposed having an identical crystal structure as $SrZrO_3$ [17], in this paper, we systematically present a first-principles study of the structural, dielectric and dynamical properties of the different phases of $SrHfO_3$, as has not yet been done to our knowledge, compared to the study of $SrZrO_3$ [18]. In the cubic phase, our calculations highlight the coexistence of both antiferrodistortive (AFD) and ferroelectric (FE) structural instabilities, previously founded by Vali [10] and Sinha [19] but overlooked by Yangthaisong [20]. We then characterize the orthorhombic ground state as well as many possible intermediate phases and compare their internal energies. We finally discuss the main features of the FE instability and conclude that it is not possible to induce FE ground state either by compressive or tensile epitaxial strain. Our comparative study between the two perovskites will serve to give a deeper understanding of underlying physics of this compound.

This paper is organized as follows. Section II summarizes the technical details of the calculations. Section III presents the lattice constant, the Born effective charges and phonon dispersion curves of the cubic perovskite phase. Section IV discusses the AFD instabilities and the relative stability of different possible phases arising from the condensation of these instabilities. Section V discusses the FE instability and the possibility to induce the ferroelectric instabilitity in the *Pnma* ground state. Section VI concludes the paper.

2. Technical details

The first-principles calculations presented in this work were performed in the framework of density functional theory (DFT) thanks to the ABINIT package [21,22]. The exchange-correlation term is described by adopting generalized gradient approximation using the Perdew-Burke-Ernzerhof of revised for solids functional (GGA–PBESol) [23]. We adopted a plane-wave pseudopotential approach, with optimized pseudopotentials generated using the ONCVPSP code [24,25]. The 4*s*, 4*p*, and 5*s* levels of Sr, 5*s*, 5*p*, 5*d*, and 6*s* levels of Hf, and 2*s* and 2*p* levels of O were considered as valence states. Some results have been checked at the LDA level using Slater exchange [26]. Convergency was reached for

E-mail address: safari.amisi@uliege.be.

https://doi.org/10.1016/j.cocom.2019.e00383
2352-2143/

Table 1
Reported phase transition in $SrHfO_3$ compared to $SrZrO_3$: Exp.1: X-ray diffraction, Exp.2: Neutron diffraction. The phase transition temperature is from *Pnma* ground state. Whatever the reported structural phase transition, the ground state is definitely the *Pnma* phase.

$SrHfO_3$			$SrZrO_3$
Theor. [10]	Exp.1 [5,7]	Exp.2 [6,8]	Exp.1 [16]
$Pm\bar{3}m$	$Pm\bar{3}m$ (1000 K)	$Pm\bar{3}m$ (1360 K)	$Pm\bar{3}m$ (1170°C)
$I4/mcm$	*Imma* (700 K)	$I4/mcm$ (1023 K)	$I4/mcm$ (830°C)
Imma	*Pnma*	*Cmcm* (873 K)	*Imma* (700°C)
Pnma		*Pnma*	*Pnma*

an energy cutoff of 45 hartrees for the plane-wave expansion and a $8 \times 8 \times 8$ grid of *k*-points for the Brillouin zone sampling of the single perovskite cell with five atoms. When condensing the AFD instabilities, either we considered a 20-atom supercell corresponding to $2a_0$, $2a_0$, and $2a_0$, and a sampling of $6 \times 4 \times 6$ *k*-points or, for the *Cmcm* phase, a 40-atom supercell corresponding to $2a_0$, $2a_0$, and $2a_0$ and a sampling of $4 \times 4 \times 4$ *k*-points. We explicitly checked that the relative energy of the different phases is well converged and independent of the choice of the supercell. Structural relaxations were performed until the forces and stresses were smaller than 10^{-7} hartrees/bohr and 10^{-7} hartrees/bohr^3 respectively. The phonon frequencies, Born effective charges, and electronic dielectric tensor were calculated according to density functional perturbation theory (DFPT) [27]. The Space Group Symmetry were checked by FINDSYM program [28] and the phonon modes were analysed by AMPLIMODES code [29].

3. Cubic perovskite structure

First, we report the properties of the highly-symmetric cubic perovskite structure of $SrHfO_3$. In this cubic phase, the atomic positions are fixed by symmetry and the only structural parameter to be relaxed is the lattice constant a_0. Our results are reported in Table 2 compared to $SrZrO_3$, $SrTiO_3$ and $CaTiO_3$, and other theoretical and experimental values. We report also the Born effective charges (Z^*) and the optical dielectric constant (ε^∞) of cubic $SrHfO_3$, $SrZrO_3$, $SrTiO_3$ and $CaTiO_3$. In the cubic structure, Z^* of *A* (*A* = Sr; Ca) and *B* (*B*= Hf; Zr; Ti) atoms are isotropic while, for O, two distinct values have to be considered depending if the O atom is displaced along the *B*–O chain ($O_\parallel$) or perpendicularly to it ($O_\perp$).

Our relaxed lattice constant ($a_0 = 4.093$ Å) is in good agreement with those reported experimentally and other theoretical results. Note that the experimental lattice constant reported varies from 4.069 Å to 4.117 Å [2–8]. All of the present ab initio calculations were performed using our calculated theoretical perovskite lattice constants. The Born effective charges of *B* (*B*= Hf; Zr; Ti) and $O_\parallel$ are strongly anomalous, 5.72/6.15/7.28/7.36*e* and −4.57/−4.99/−5.76/−5.87*e* instead of the nominal charges of respectively +4*e* and −2*e*. These anomalous Born effective charges are known as a common feature of ABO_3 compounds and were related to dynamical transfer of charge between the B *d* and O 2*p* orbitals [31]. $Z^*_{Sr/Ca}$ and $Z^*_{O_\perp}$ are also anomalous but to a much lower extent. We notice the trend for the Born effective charges of larger beings in titanates ($ATiO_3$) than in zirconates ($AZrO_3$) and hafnates ($AHfO_3$). The Z^* of $SrHfO_3$ are in fact closer to those of $SrZrO_3$ than to those of $SrTiO_3$ and $CaTiO_3$ [18]. The calculated optical dielectric constant is of 4.38, near to that for $SrZrO_3$ (4.71). It is smaller than for $ATiO_3$ (*A* = Sr, 6.24; Ca, 6.39), coherently with the larger bandgap of $SrZr-HfO_3$.

Within our calculations $SrHfO_3$ is described as a good insulator with an indirect bandgap of 3.76 eV between *R* and Γ points, which is closer to that of $SrZrO_3$ (3.42 eV) and consistent with other results (3.74 eV [11], 3.61 eV [20], 3.7 eV [32]) but wider than that of $SrTiO_3$ (1.88 eV). The feature of the GGA is, among others, to underestimates from about 30 to 40%, the experimental band gap, which is 6.1 eV [30] but correctly reproduces the insulating nature of this compound. Note, however, that the hybrid functionals, like B3PW and B3LYP give a bandgap value much better agreement with the experiment, as demonstrated by Eglitis *et al.* on the $SrZrO_3$ (Exp.: 5.60; B3PW: 5.30; B3LYP: 5.31) [33,34].

In Fig. 1, we report the phonon dispersion curves of cubic $SrHfO_3$. The Γ–*X*, Γ–*M*, and Γ–*R* lines are along the [100], [110], and [111] directions, respectively. Negative values in the graph correspond to

Table 2
Lattice parameter (Å) of $SrHfO_3$ at relaxed volume compared to $SrZrO_3$ and $SrTiO_3$, and other theoretical and experimental values. [a]: GGA–PBESol, [b]: LDA, [c]: GGA–WC. Born effective charges (|*e*|), optical dielectric tensor and GAP of cubic $SrHfO_3$ and $SrZrO_3$. The nominal charge are +2|*e*|, +4|*e*|, and −2|*e*| for *A*, *B* and *O* ions respectively.

	$SrHfO_3$		$SrZrO_3$		$SrTiO_3$	$CaTiO_3$
	Theortical		Exp.	18	Present	18
	Present	LDA [11]				
a_0	4.093[a]		4.114 [6]	4.126[c]	3.888[a]	3.854[c]
	4.048[b]	4.057		4.046[b]		
Z^*_A	2.58	2.58		2.58	2.56	2.58
Z^*_B	5.72	5.73		6.15	7.28	7.36
$Z^*_{O_\parallel}$	−4.57	−4.55		−4.99	−5.76	−5.87
$Z^*_{O_\perp}$	−1.86	−1.87		−1.87	−2.04	−2.03
ε^∞	4.38	4.43		4.71	6.24	6.39
GAP	3.76	3.74	6.1 [2,30]	3.42	1.88	

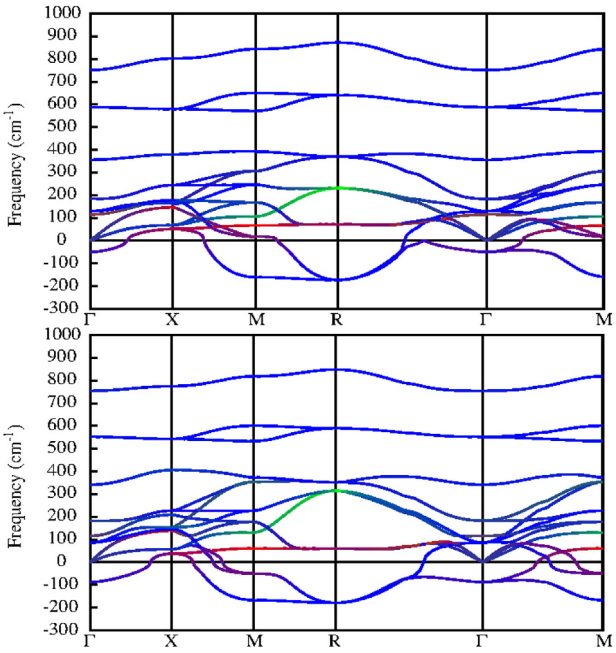

Fig. 1. (Color online) Calculated phonon dispersion curves of cubic (a) $SrHfO_3$, and (b) $SrZrO_3$ [18] at the GGA–PBESol and GGA-WC volumes respectively along the path $\Gamma - X - M - R - \Gamma - M$ of the cubic Brillouin zone.

imaginary phonon frequencies and are related to unstable modes. By condensing these unstable modes, it is theoretically possible to find the possible intermediate phases and the stable phase of a compound. Frequencies and types ferroic unstable modes are summarized in Table 3.

We see in Fig. 1 and Table 3 that there are strong AFD instabilities at the R point (R_4^+, 173i cm^{-1}, triply degenerated) and at the M point (M_3^+, 160i cm^{-1}, not degenerated). These modes correspond to rotations of oxygen octahedra as it will be discussed in the next Section. The present calculation of zone center phonons of cubic $SrHfO_3$ shows an unstable TO mode as an imaginary frequency mode with the value of 49i cm^{-1}, in agreement with what has been predicted by Stachiotti *et al.* [9] (76i cm^{-1}), Vali [10] (61i cm^{-1}), Hou [11] (66.9i cm^{-1}) and Sinha [19] (75i cm^{-1}). This Γ_4^- unstable mode was not observed by Yangthaisong [20] who worked within the LDA−PZ and GGA−PBE. Our LDA calculation reveals an additional instability at the point M (M_5^-, 5i cm^{-1}, twice degenerated), in agreement with the phonon curves presented by Vali [10] but very weak compared to the same instability shown in $SrZrO_3$ [18] (M_5^-, 50i cm^{-1}). The Γ_4^- instability is a polar TO mode that involves the motions of Sr, Hf and O atoms while the M_5^- unstable mode involves the anti-polar motion of Sr and O atoms. Comparatively to the phonon dispersion curves of cubic $SrZrO_3$, which exhibits the same *Pnma* orthorhombic antiferrodistorted ground state, we notice that the phonon dispersion curves of $SrHfO_3$ are similar to those of $SrZrO_3$, particularly for AFD modes: they shows an AFD instability extending from M to R as well as Γ_4^- unstable mode. The only important difference is the amplitudes of the instabilities that are larger in $SrZrO_3$ (Γ_4^-: 87i cm^{-1}; R_4^+: 179i cm^{-1}; M_3^+: 167i cm^{-1}; M_5^-: 50i cm^{-1}) than in $SrHfO_3$ especially for the Γ mode (4% for AFD and 44% for FE). This result will be useful later in the text.

Let's now analyse in the next two Sections the AFD instabilities and the related orthorhombic ground-state structure. We will then discuss the FE instabilitity.

4. Antiferrodistortive instabilities

The AFD R_4^+ and M_3^+ modes were observed in the phonon dispersion curves in the $SrHfO_3$ paraelectric cubic phase (Fig. 1), with more larger amplitudes imaginary frequencies (173i cm^{-1} and 160i cm^{-1}, respectively, Table 3) than FE mode (Γ_4^-, 49i cm^{-1}). R_4^+ and M_3^+ define unstable modes that are associated to tilts of the oxygen octahedra along one of the three cubic directions, with consecutive octahedra along that direction moving either “in phase” (M_3^+ tilts) or “out-of-phase” (R_4^+ tilts). These motions correspond to the tilt components identified by Glazer [35,36] and that can be combined to generate more complex tilted structures. So, what phase stabilize the $SrHfO_3$ it was only AFD? In order to identify the AFD ground state of $SrHfO_3$, we computed the energy gains arising from the consecutive appearance of different tilts in the reference cubic perovskite structure belongs to the space group $Pm\bar{3}m$, wich is described in Glazer's notations as $a^0a^0a^0$. Of course, as we can see in Fig. 3, the full relaxation of distortions combining the two oxygen rotation modes M_3^+ and R_4^+ favor the appearance of several additional modes, even though they are not unstable by themself [37,38]. Although the different relaxed structures can consequently only be described in first approximation as arising from a combination of perfect tilts, we will still refer to them below through the well-know Glazer's notations for convenience.

In Fig. 2, we report for the AFD phases the energy gain calculated with two functional, GGA−PBESol and LDA, compared to the high symmetry cubic phase. To analyse the effect of the functional, the strain and the cation displacement on energy gain for *Imma*, *Cmcm* and *Pnma* phases, we did three calculations: The first calculation, we'll call the current calculation (cal. 1), in GGA−PBESol and LDA, was to allow the relaxation of the strain, i.e. by making a complete relaxation lattice parameters and atomic positions, in the second calculation (cal. 2) we were relaxing only atomic positions in the cubic volume (cubic lattice parameter fixed), i.e. by not allowing the strain to relax, and the third type of calculation (cal. 3), meanwhile, was to also relax the lattice parameters and atomic positions, as for the calculation (cal. 1), but by setting the cations to their high symmetry positions. The calculations (cal. 2) and (cal. 3) were done only using the functional GGA−PBESol.

Comparing the energy gains of the two separate AFD modes (R_4^+ and M_3^+), we note that the M_3^+ instability is energetically disadvantaged compared to the ones of R_4^+ in the $SrHfO_3$. The relaxation of the M_3^+ mode is more favorable when it is condensed around a single direction ($a^0a^0c^+$, $P4/mbm$, −138 meV/f.u.) than in three directions ($a^+a^+a^+$, $Im\bar{3}$, −134 meV/f.u.), whereas for the R_4^+ mode, our calculations show that it is more favored when it is condensed simultaneously around two directions. The *Imma* phase ($a^-a^-c^0$, −195 meV/f.u.) is indeed lower in energy than the phases $I4/mcm$ ($a^0a^0c^-$, −176 meV/f.u.), “out-of-phase” rotation around a single direction, and $R\bar{3}c$ ($a^-a^-a^-$, −185 meV/f.u.), “out-of-phase” rotation around three directions. Even by adding a FE motion in the last phase, which gives $R3c$ ($a_p^-a_p^-a_p^-$), whatever the functional used (red, GGA−PBESol, and blue, LDA, columns), we still do not observe any additional energy gain (−185 meV/f.u.).

By now combining the two modes of rotation M_3^+ and R_4^+, we note, in agreement with the analyzes of the previous individual condensations, the unfavorable character of the condensation of “in phase” rotations (M_3^+) in two directions, with the *Pnmm* phase ($a^-b^+b^+$, −183 meV/f.u.) slightly higher in energy than the *Cmcm* phase ($a^0b^-c^+$, −185 meV/f.u.). The R_4^+ mode contribution can be seen when compared $Im\bar{3}$, with “in phase” rotations in three directions ($a^+a^+a^+$), and *Pnmm*, replacing only one “in phase” by an “out-of-phase” rotation ($a^-b^+b^+$), that produce a gain of energy about −50 meV/f.u. So, whatever the functional used (red, GGA−PBESol, and blue, LDA, columns), we notice that *Cmcm* phase ($a^0b^-c^+$, −185 meV/f.u.) appear to be more favorable in $SrHfO_3$ than $Im\bar{3}$ ($a^+a^+a^+$, −134 meV/f.u.), *Pnmm* ($a^-b^+b^+$, −183 meV/f.u.), $R\bar{3}c$ ($a^-a^-a^-$, −185 meV/f.u.) and $R3c$ ($a_p^-a_p^-a_p^-$, −185 meV/f.u.) phases. Let's put aside the last four phases, since they are unlikely, and continue our analysis about the other more favorable phases in

Table 3
Modes and soft phonon frequencies ω (cm^{-1}) of $SrHfO_3$ cubic at Γ, M and R points of the Brillouin zone, compared to $SrZrO_3$ [18]. AP = antipolar mode.

k-points		Mode	Type	ω (cm^{-1})		
				$SrHfO_3$		$SrZrO_3$
				GGA−PBEsol	LDA	GGA−WC
Γ	(0, 0, 0)	Γ_4^-	(FE)	3 × 49i	3 × 55i	3 × 87i
M	(½, ½, 0)	M_3^+	(AFD)	1 × 160i	1 × 169i	1 × 167i
		M_5^-	(AP)	0i	2 × 5i	2 × 50i
R	(½, ½, ½)	R_4^+	(AFD)	3 × 173i	3 × 183i	3 × 179i

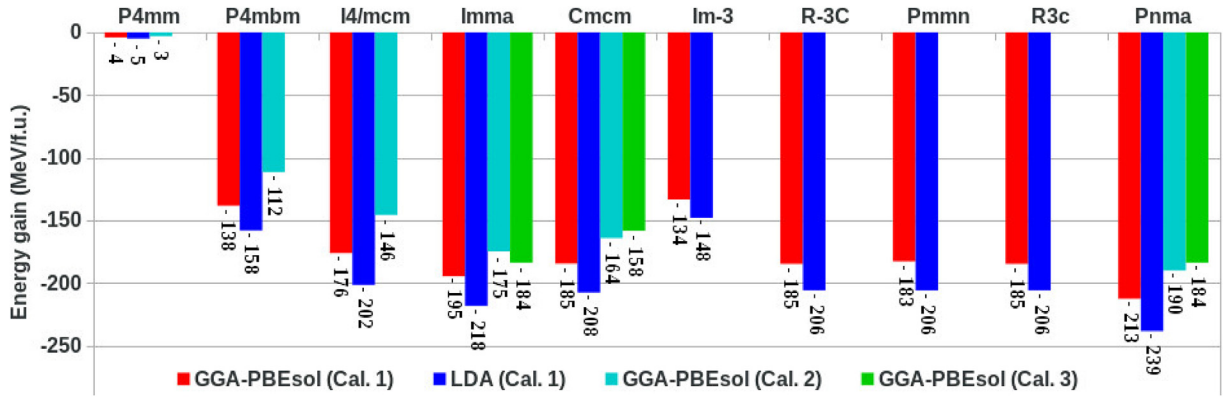

Fig. 2. (Color online) Calculated energy gain (in meV/f.u.) with respect to the cubic phase of different phases of $SrHfO_3$. Relative total energies are shown with $Pm\bar{3}m$ phase as the reference. The energies were calculated with two functional, GGA−PBESol and LDA, and consist here of three calculations, (cal. 1: red columns for GGA−PBESol, and blue columns for LDA), (cal. 2: cyan columns) and (cal. 3: green columns), as described in the text. For clarity, the exact value of the energy gain is written in each case. The two functional ones show the same sequence for all phases.

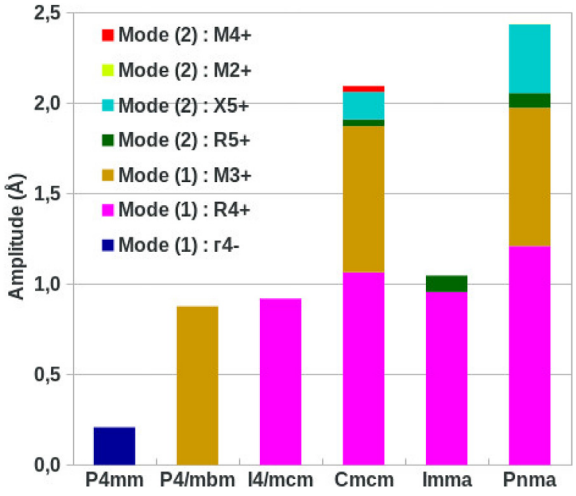

Fig. 3. (Color online) Modes contributing to the condensation of relaxed main phases in $SrHfO_3$. Associated amplitudes (in Å) were calculated by AMPLIMODES [29]. The main modes consist of FE displacement (Γ_4^-) and oxygen octahedron rotation (R_4^+ and M_3^+), whereas the additional modes consist of couplings with cations (R_5^+ and X_5^+) or oxygens (M_2^+ and M_4^+) displacements. At the scale of this diagram, the contribution of the mode M_2^+, in *Pnma* phase, is insignificant.

$SrHfO_3$ (*I*4/*mcm*, *Imma*, *Cmcm*, and *Pnma*).

Similarly to what was found in the $SrZrO_3$, the *Cmcm* and *Imma* phases have similar internal energy, with only a difference of −10 meV/f.u. to the advantage of the *Imma* phase. Comparing the first two calculations (cal. 1), making a complete relaxation lattice parameters and atomic positions (red columns), and (cal. 2), not allowing the strain to relax (cyan columns), we can observe a sizeable contribution of strain relaxation: −30 meV/f.u. in *I*4/*mcm* and about −20 meV/f.u. in *Cmcm*, *Imma* and *Pnma* phases. Considering the third type of calculation (cal. 3), by setting the cations to their high symmetry positions (green columns), we find that the two phases *Imma* and *Pnma*, with equal energy (−184 meV/f.u.) are energetically more favorable in $SrHfO_3$ than *Cmcm* (−158 meV/f.u.) phase, thus giving the *Imma* phase a not insignificant position. The *Imma* phase is not yet observed experimentally but it seem to be more favorable in $SrHfO_3$ than that *Cmcm* experimentally reported [6,8]. The contribution of cations relaxation is more observed in *Pnma* (−29 meV/f.u.) and *Cmcm* (−27 meV/f.u.) than in *Imma* (−11 meV/f.u.). According to the energy gain obtained in each of the AFD phases presented in Fig. 2, it turns out that, whatever the fu > nctional used, the purely low-energy AFD state in $SrHfO_3$ is in the orthorhombic phase *Pnma* ($a^-b^+a^-$), combining two "out-of-phase" rotations (R_4^+) and an "in phase" rotation (M_3^+). The coupling of these two modes of rotation has the effect inter alia of reducing their amplitudes of octahedral rotations: c^+= 11.68° in *P*4/*mbm*, c^-= 12.24° in *I*4/*mcm*, whereas b^+= 7.19° and a^-= 8.05° in the *Pnma* phase.

Our result (Fig. 2) shows the sequence $Pm\bar{3}m$>*P*4*mm* > *P*4/*mbm* > *I*4/*mcm* > *Cmcm* > *Imma* > *Pnma*, in agreement with that ($Pm\bar{3}m$ > *I*4/*mcm* > *Cmcm* > *Pnma*) founded by Kennedy et al. [6] and Murata et al. [13]. We note here a remarkable similarity between the two compounds $SrHfO_3$ and $SrZrO_3$ as regards the hierarchy of the distortions as a function of the internal energy [18]. It is interesting that this hierarchy is different from that reported by Vali [10], in which $Pm\bar{3}m$ > *Cmcm* > *I*4/*mcm* > *Pnma*, reporting *Cmcm* less stable than *I*4/*mcm*, and by Cherrad et al. [39], in which $Pm\bar{3}m$ > *I*4/*mcm* > *Imma* > *Cmcm* > *Pnma*, reporting *Cmcm* less stable than *Imma*. To quantify the distortions that appear in the main phases we project the structural distortions onto symmetry adapted modes of the cubic phase using AMPLIMODE software [29]. The results in Fig. 3 show the amplitudes of the modes in the fully relaxed phases from the calculations.

In the *P*4*mm*, *P*4/*mbm*, and *I*4/*mcm* phases the mode decomposition shows only the primary modes we have condensed: Γ_4^- (blue column), M_3^+ (yellow columns), and R_4^+ (magenta columns) respectively (Fig. 3). This is different for the *Imma*, *Cmcm*, and *Pnma* phase in which the additional modes R_5^+ (green columns), X_5^+ (cyan columns), M_2^+ and M_4^+ (red column) appears, through trilinear couplings with antipolar modes type $\lambda Q_{M_3^+} Q_{R_4^+} Q_{X_5^+}$ or $\lambda Q_{M_3^+} Q_{R_4^+} Q_{R_5^+}$ [18], with a small amplitude in the mode projections while we have condensed only the primary R_4^+ and M_3^+ modes. In the *Imma* phase the coupling, allowed by the (cal. 1) with respect to the (cal. 3), is done with the R_5^+ mode and allow substantial additional energy gain (−11 meV/f.u., Fig. 2). In the *Cmcm* and *Pnma* phases, coupling with the R_5^+ mode is also allowed, but it is mainly a coupling with the X_5^+ mode (Fig. 3) which becomes dominant and stabilizes these phases through additional energy gain of respectively −27 and −29 meV/f.u. (Fig. 2). The *Pnma* structure allows the R_5^+, X_5^+ and M_2^+ (with a very low amplitude for the last) modes, and the *Cmcm* structure allows the R_5^+, X_5^+ and M_4^+ modes. In the *Pnma* phase, the atoms Hf (*B* in general case) remain fixed at their high symmetry positions. The X_5^+ mode stabilizing *Cmcm* and *Pnma* phase consist of an antipolar distortion of Sr and O atoms, with a double

contribution of Sr, in the *b* and *a* orthorhombic plane respectively, while R_5^+ mode stabilizing the *Imma* phase also consist of an antipolar displacement of Sr and O atoms, again with a double contribution of Sr, but in the orthorhombic *c* direction for Sr and $O_\perp$ plus the motion of $O_\parallel$ in the orthorhombic *a* direction.

In Table 4 we report the lattice parameters and atomic positions (in reduced coordinates) of the different possible intermediate phases. The amplitudes of the rotation angles of the oxygen octahedra are also reported. As previously mentioned, due to anharmonic couplings, some of these structures cannot be described using rigid oxygen tilts only but can involve other types of oxygen or cationic motions. The amplitudes of the rotation angles are therefore only indicative and were estimated from the amplitudes of the overlaps of the atomic distortion with rigid oxygen tilt motions. Going from single condensation (*P*4/*mbm* and *I*4/*mcm* phases) to the combination of both oxygen rotation modes R_4^+ and M_3^+ (*Cmcm* and *Pnma*), we observe that the amplitude of M_3^+ slightly decreases (−8% and −13% respectively) while the amplitude of R_4^+ increases (+16% and +32% respectively).

The sequence of the phases found in the $SrHfO_3$ is the same as that found in the $SrZrO_3$ [18]. The *I*4/*mcm* phase has a tetragonality of 1.023, slightly similar to that 1.025 for $SrZrO_3$, in good agreement with the experimental observations of Kennedy et al. [6] ($c_0/a_0 > 1$). The hierarchy of the amplitudes of the rotations is the same in the two compounds when we go from a AFD phase with one rotation towards phases with several rotations. No experimental data are available for the *Imma* phase, but the pseudotetragonality of 0.993, equal to that founded in $SrZrO_3$, is in agreement with other theoretical results [10,39]. It's in the orthorhombic *Pnma* ground state that the reduction of the amplitudes of the rotations is greatest ($a^- = 8.21^\circ$ and $b^+ = 7.20^\circ$), just as it was found in the $SrZrO_3$ ($a^- = 8.48^\circ$ and $b^+ = 7.62^\circ$).

5. Ferroelectric instability

In the phonon dispersion curves of the cubic phase (Fig. 1), we have identified a small FE instability at the zone center (Γ_4^-, 49*i* cm^{-1}). Although this instability does not play any role in the ground state, it is inherent to the material and will compete with the AFD. In this Section, we better characterize this FE instability and report how $SrHfO_3$ would behaves in absence of AFD instabilities. In Table 5 we report the tolerance factor [40] (*t*), normalized

Table 4
Calculated cell parameters and atomic positions of different phases of $SrHfO_3$, in agreement with the energy gain hierarchy observed previously. The values in bracket correspond to the experimental measurements from Ref. 6.

			a	*b*	*c*	Distortion amplitude	Rotation Angle
$a^0a^0a^0$ ($Pm\bar{3}m$)	cell (Å)		4.0929 (4.1138)	4.0929 (4.1138)	4.0929 (4.1138)		
	Sr	1(b)	½	½	½		
	Hf	1(a)	0	0	0		
	O_1	3(d)	½0 0				
$a^0a^0c^+$ (*P*4/*mbm*)	cell (Å)		5.7055	5.7055	4.1273	δ_{O2}= 0.0536	c^+: 11.68°
	Sr	2(c)	0		½	½	
	Hf	2(a)	0	0	0		
	O_1	2(b)	0	0	½		
	O_2	4(g)	$\frac{3}{4}-\delta_{O_2}$	$\frac{1}{4}-\delta_{O_2}$	0		
$a^0a^0c^-$ (*I*4/*mcm*)	cell (Å)		5.7002 (5.7907)	5.7002 (5.7907)	8.2443 (8.2121)	δ_{O2}= 0.056 (0.033)	c^-: 12.24°
	Sr	4(b)	0		½	1/4	
	Hf	4(c)	0	0	0		
	O_1	4(a)	0	0	1/4		
	O_2	8(h)	$\frac{1}{4}-\delta_{O_2}$	$\frac{3}{4}-\delta_{O_2}$	0		
$a^0b^+c^-$ (*Cmcm*)	cell (Å)		8.0721 (8.253)	8.1739 (8.266)	8.1242 (8.271)	$\delta_{Sr_{1y}}$ = 0.006 (0.062) $\delta_{Sr_{2y}}$ = 0.010 (0.001)	b^+: 7.60° c^-: 10.02°
	Sr_1	4(c)	0	$-\delta_{Sr_{1y}}$	1/4	δ_{O1x}= 0.036 (0.024)	
	Sr_2	4(c)	0	$\frac{1}{2}-\delta_{Sr_{2y}}$	1/4	δ_{O2y}= 0.034 (−0.009)	
	Hf	8(d)		1/4	1/40	δ_{O2z}= 0.045 (0.041)	
	O_1	8(e)	$\frac{3}{4}+\delta_{O_{1x}}$ 0	0	$\delta_{O_{3x}}$ = 0.047 (−0.031)		
	O_2	8(f)	0	$\frac{1}{4}+\delta_{O_{2y}}$	$-\delta_{O_{2z}}$	δ_{O3y}= 0.004 (0.016)	
	O_3	8(g)	$\frac{1}{4}-\delta_{O_{3x}}$	$\frac{1}{4}+\delta_{O_{3y}}$	1/4		
$a^-a^-c^0$ (*Imma*)	cell (Å)		8.0778	5.7510	5.7697	δ_{Srz}= 0.010	a^-: 9.00°
	Sr	4(e)	0	1/4	$\frac{1}{4}+\delta_{Sr_z}$	$\delta_{O_{1z}}$ = 0.079	
	Hf	4(d)	1/4	1/4	3/4	δ_{O2x}= 0.043	
	O_1	4(e)	0	1/4	$\frac{3}{4}+\delta_{O_{1z}}$		
	O_2	8(f)	$\frac{3}{4}-\delta_{O_{2x}}$	0	0		
$a^-b^+a^-$ (*Pnma*)	cell (Å)		5.7621 (5.7646)	8.1053 (8.1344)	5.7261 (5.7516)	δ_{Sr_x} = 0.028 (0.016) δ_{Sr_z} = 0.006 (0.004)	b^+: 7.19° a^-: 8.05°
	Sr	4(c)	δ_{Sr_x}	1/4	$\frac{1}{2}+\delta_{Sr_z}$	$\delta_{O_{1x}}$ = 0.016 (0.014)	
	Hf	4(a)	0	0	0	$\delta_{O_{1z}}$ = 0.072 (−0.063)	
	O_1	4(c)	$-\delta_{O_{1x}}$	1/4	$\delta_{O_{1z}}$	$\delta_{O_{2x}}$ = 0.033 (0.029)	
	O_2	8(d)	$\frac{1}{4}+\delta_{O_{2x}}$	$\delta_{O_{2y}}$	$\frac{3}{4}+\delta_{O_{2z}}$	$\delta_{O_{2y}}$ = 0.038 (0.036) $\delta_{O_{2z}}$ = 0.033 (−0.031)	

eigendisplacement in real space for FE unstable mode at Γ point (polarization along z) and TO modes effectives charge associated (as defined in Ref. 27).

When consider the ATiO$_3$ perovskites (ferroelectrics PbTiO$_3$ and BaTiO$_3$, and incipient ferroelectric SrTiO$_3$) in the cubic phase, the eigendisplacement vector of the Γ polar instability is dominated by opposite displacements of B and O atoms (O$_\parallel$ and O$_\perp$), while for AFD perovskites SrBO$_3$ (B = Zr; Hf), the B and O$_\parallel$ displacement contribution become smaller and the Γ polar instability is relatively dominated by opposite displacements of A and O$_\perp$ atoms. In the SrBO$_3$ (B = Zr; Hf), contrary to what is observed in the ATiO$_3$ perovskites, the B now appears to move not *against* but *with* the oxygens but with a much smaller amplitude. The weak Sr−Hf displacements contribution in SrHfO$_3$, compared to Sr-Zr contributions in SrZrO$_3$, can be explained by the fact that the atomic weight of Hf is approximately twice that of Zr, 178.5 vs 91.2 amu. The mode effective charge associated with this unstable mode is 4.15e, close to that in SrZrO$_3$ (4.38e), while this value increase in ATiO$_3$.

From the analysis of Table 5, we see that the balance of A or B sites in the condensation of pure FE mode and the intensity of modes effective charge vary with the Goldschmidt tolerance factor t. The ATiO$_3$ compounds all have a tolerance factor $t > 1$ and an eigenvector dominated by the B cation (AB for PbTiO$_3$), while in the SrBO$_3$ (B = Zr; Hf) AFD compounds with a tolerance factor $t < 1$, the instabilities are more dominated by the A cation (AB for SrHfO$_3$). In terms of the tolerance factor, SrTiO$_3$ (1.001) is in between the ferroelectric BaTiO$_3$ (1.063) and SrHfO$_3$ (0.949), which exhibits octahedral rotations, showing that the crystal is on the borderline of being AFD or FE. Indeed SrTiO$_3$ is known to be an incipient ferroelectric [41]. The compound with a strong A-site dominance is rather AFD at low energy state, such as SrHfO$_3$ and SrZrO$_3$ which stabilizes the AFD orthorhombic phase *Pnma* with small mode effective charge. The O$_\parallel$ displacement is low in AFD compounds, and relatively beyond the triple in ATiO$_3$, which is characteristic of oxygen rotations in the former.

In the cubic symmetry, FE unstable mode is three times degenerate. We then compared the energies of phases with the polarization along three different directions in order to identify the FE polar phase lowest energy: FE$_z$ (*P4mm*) phase with a polarization oriented in the [100] direction, FE$_{xy}$ (*Amm*2) phase with a polarization oriented in [110] direction and FE$_{xyz}$ (*R*3*m*) with a polarization along the diagonal [111]. We present in Fig. 4 energy gains from the cubic phase high symmetry and polarization of the three FE polar phases related in SrHfO$_3$, respectively. To analyse the effect of the strain on energy gain for polar phases, we did two calculations: The (cal. 1), for GGA−PBESol and LDA, and the (cal. 2) as previously explained.

From the energies, similarly to that founded in SrZrO$_3$ [18], the SrHfO$_3$ FE$_z$ phase is the most stable, meaning that in the absence of AFD instabilities the resulting ground state would be a ferroelectric *P4mm* tetragonal phase, as predicted by Sinha [19] and Murata et al. [13]. Whatever the type of calculation carried out, LDA and GGA−PBESol, (cal. 1) and (cal. 2), the *P4mm* trend remains confirmed. While in the SrZrO$_3$ strain relaxation favors the stable FE tetragonal state [18], in the SrHfO$_3$ the strain does not seem to play a significant role in stabilizing the same stable FE tetragonal state. Vali [10] has conclude that *P4mm* and *Cmcm* phases of SrHfO$_3$ cannot possibly occur.

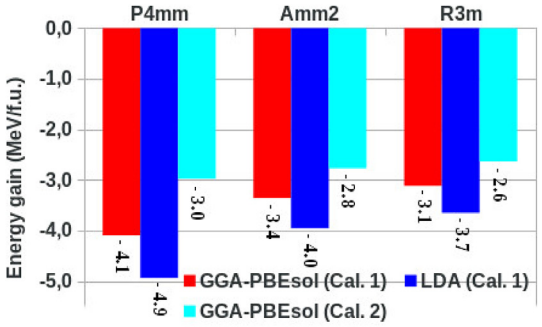

Fig. 4. (Color online) Gain of energy with respect to the paraelectric reference (meV/f.u.) for ferroelectric distortions in SrHfO$_3$. For clarity, the exact value of the energy gain is written in each case. The energies were calculated with two functional, GGA−PBESol and LDA, and consist of two calculations as explained in the text.

The possibility of inducing ferroelectricity by strain engineering in the *Pnma* ground state of the SrZrO$_3$ has been demonstrated by Amisi et al. [18]. What about SrHfO$_3$? Using the same methodology as that was done in SrZrO$_3$, we suppose a cubic perovskite substrate imposing to the *Pnma* phase of SrHfO$_3$ an epitaxial constraint $a = c = \sqrt{2}a_{\text{substrate}}$, limiting also ourselves to epitaxial strains of ±4% (with respect to the pseudocubic cell parameter) which typically correspond to the largest values accessible experimentally on this type of system. For each calculation, the cell parameter b is relaxed together with the atomic positions. Two cases was considered: the case of a compressive epitaxial strain of −4% ($a_{\text{substrate}} = 3.899$ Å), and the one of a tensile epitaxial strain of +4% ($a_{\text{substrate}} = 4.224$ Å). According to our calculations, the structure stays in the $a^-b^+a^-$ phase, confirmed by the absence of any further phonon instability, with just a modification of the amplitude of the AFD distortions and an expansion or contraction of the cell along the b direction. It therefore appears that, contrary to SrZrO$_3$, it is not possible to induce a FE-*Pnma* ground state in SrHfO$_3$ by imposing either a compressive or a tensile epitaxial strain.

6. Conclusions

In this paper, we reported a first-principles study of the structural and dynamical properties of SrHfO$_3$. We pointed out that, in its cubic phase, SrHfO$_3$ exhibits both antiferrodistortive and ferroelectric instabilities. The antiferrodistrotive instabilities are responsible for the *Pnma* ground-state, that arises from the successive condensation of three rotational modes and further prevent the appearance of a ferroelectric distortion. Our results showed that the *Imma* and *Cmcm* phases have a very similar internal energy but it is the *Imma* phase which is the most stable. We have highlighted that in absence of AFD distortions, SrHfO$_3$ would be a *P4mm* tetragonal ferroelectric with a spontaneous polarization of 23 μC/cm^2, smaller than in SrZrO$_3$ (42 μC/cm^2). The hierarchy of phases with respect to the internal energy of the SrHfO$_3$ is the same as in the SrZrO$_3$, but contrary to what was found for last, it seems to us very unlikely to induce the ferroelectricity in the SrHfO$_3$ *Pnma* ground state either by compressive or tensile epitaxial strain.

Table 5
Tolerance factor [40] (t), normalized eigendisplacement in real space for FE unstable mode at Γ point (polarization along z) and TO modes effectives charge associated (as defined in Ref. 27). The dynamic matrix of eigenvectors associated can be obtained by multiplying each value by the appropriate mass factor $\sqrt{M_i}$. Values in parentheses represent the contribution of each atom (knowing that there are two anions O$_\perp$), in %, to total displacement, calculated according to its eigendisplacement and mass, with $\sum n_i^2.M_i = 1$. (^{a}): present, (^{b}): Ref. 18, (^{c}): Ref. 38.

ABO_3	t	A	B	O$\parallel$	O$_\perp$	$\overline{Z}^*$
SrHfO$_3$(^{a})	0.949	+0.079 (*11*)	−0.015 (*08*)	−0.049 (*08*)	−0.108 (*37*)	4.15
SrZrO$_3$(^{b})	0.942	+0.068 (*41*)	−0.010 (*01*)	−0.060 (*06*)	−0.128 (*26*)	4.38
SrTiO$_3$(^{a})	1.001	+0.030 (*08*)	+0.067 (*22*)	−0.114 (*21*)	−0.125 (*25*)	7.77
PbTiO$_3$(^{c})	1.001	+0.017 (*06*)	+0.054 (*14*)	−0.120 (*23*)	−0.133 (*28*)	8.19
BaTiO$_3$(^{c})	1.063	+0.001 (*00*)	+0.098 (*45*)	−0.147 (*35*)	−0.078 (*10*)	9.34

Acknowledgments

This work was partially supported by the Wallonie-Bruxelles International (WBI, Grant numbers: SOR/2015/230351). Calculations have been performed by the CECI supercomputing center [42].

References

[1] K. Rabe, C. Ahn, J.-M. Triscone, Physics of Ferroelectrics: A Modern Perspective, Springer, Berlin, 2007.
[2] C. Rossel, M. Sousa, C. Marchiori, J. Fompeyrine, D. Webb, D. Caimi, B. Mereu, A. Ispas, J.P. Locquet, H. Siegwart, R. Germann, A. Tapponnier, K. Babich, Microelectron. Eng. 84 (2007) 1869. https://doi.org/10.1016/j.mee.2007.04.029.
[3] M. Sousa, C. Rossel, C. Marchiori, H. Siegwart, D. Caimi, J.-P. Locquet, D.J. Webb, R. Germann, J. Fompeyrine, K. Babich, J.W. Seo, Ch Dieker, J. Appl. Phys. 102 (2007) 104103. https://doi.org/10.1063/1.2812425.
[4] E.V. van Loef, W.M. Higgins, J. Glodo, C. Brecher, A. Lempicki, V. Venkataramani, W.W. Moses, S.E. Derenzo, K.S. Shah, IEEE Trans. Nucl. Sci. 54 (No. 3) (2007). https://doi.org/10.1109/TNS.2007.896343.
[5] S.L. Cuffini, J.A. Guevara, Y.P. Mascarenhas, P. de la Presa, A. Ayala, A. López-García, Cerâmica 43 (No. 280) (1997) 91–94. https://www.researchgate.net/profile/Patricia_De_la_Presa.
[6] B.J. Kennedy, C.J. Howard, B.C. Chakoumakos, Phys. Rev. B 60 (1999) 2972. https://doi.org/10.1103/PhysRevB.60.2972.
[7] P. de la Presa, R.E. Alonso, A.P. Ayala, V.V. Krishnamurthy, K.P. Lieb, A. López-García, M. Neubauer, M. Uhrmacher, Hyperfine Interact. 120/121 (1999) 479–483, https://doi.org/10.1023/A:1017061826092.
[8] M.K. Singh, G. Singh, T.H. Kim, S. Kojima, R.A. Katiyar, J.F. Scott, Europhys. Lett. 107 (2014) 26004. https://doi.org/10.1209/0295-5075/107/26004.
[9] M.G. Stachiotti, G. Fabricius, R. Alonso, C.O. Rodriguez, Phys. Rev. B 58 (1998) 8145. https://doi.org/10.1103/PhysRevB.58.8145.
[10] R. Vali, Solid State Commun. 148 (2008) 29–31. https://doi.org/10.1016/j.ssc.2008.07.018.
[11] Z.F. Hou, Phys. Status Solidi B 246 (No. 1) (2009) 135–139. https://doi.org/10.1002/pssb.200844173.
[12] R. Vali, Solid State Commun. 149 (2009) 519–522. https://doi.org/10.1016/j.ssc.2009.01.012.
[13] H. Murata, T. Yamamoto, H. Moriwake, I. Tanaka, Phys. Status Solidi B 246 (No. 7) (2009) 1628–1633. https://doi.org/10.1002/pssb.200945041.
[14] L.-P. Feng, Z.-Q. Wang, Q.-J. Liu, T.-T. Tan, Z.-T. Liu, Chin. Phys. Lett. 29 (No. 12) (2012) 127103. https://doi.org/10.1088/0256-307X/29/12/127103.
[15] D.P. Rai, Sandeep, A. Shankar, A.P. Sakhya, T.P. Sinha, B. Merabet, M. Musa Saad H.-E, R. Khenata, A. Boochani, S. Solaymani, R.K. Thapa, Mater. Chem. Phys. 186 (2017) 620–626. https://doi.org/10.1016/j.matchemphys.2016.11.045.
[16] C.J. Howard, K.S. Knight, B.J. Kennedy, E.H. Kisi, J. Phys. Condens. Matter 12 (2000) L677. https://doi.org/10.1088/0953-8984/12/45/101.
[17] M. Guennou, P. Bouvier, B. Krikler, J. Kreisel, Phys. Rev. B 82 (2010) 134101. https://doi.org/10.1103/PhysRevB.82.134101.
[18] S. Amisi, E. Bousquet, K. Katcho, Ph Ghosez, Phys. Rev. B 85 (2012), 064112, https://doi.org/10.1103/PhysRevB.85.064112.
[19] M.M. Sinha, Chin. J. Phys. 49 (No. 1) (2011) 301. https://www.ps-taiwan.org/cjp/download.php?type=paper%5c%26%7b%7dvol=49%5c%26%7b%7dnum=1%5c%26%7b%7dpage=301.
[20] A. Yangthaisong, J. Electron. Mater. 41 (No. 3) (2012) 535. https://doi.org/10.1007/s11664-013-2492-4.
[21] X. Gonze, B. Amadon, P.-M. Anglade, J.-M. Beuken, F. Bottin, P. Boulanger, F. Bruneval, D. Caliste, R. Caracas, M. Cote, T. Deutsch, L. Genovese, Ph Ghosez, M. Giantomassi, S. Goedecker, D.R. Hamann, P. Hermet, F. Jollet, G. Jomard, S. Leroux, M. Mancini, S. Mazevet, M.J.T. Oliveira, G. Onida, Y. Pouillon, T. Rangel, G.-M. Rignanese, D. Sangalli, R. Shaltaf, M. Torrent, M.J. Verstraete, G. Zerah, J.W. Zwanziger, Comput. Phys. Commun. 180 (2009) 2582. https://doi.org/10.1016/j.cpc.2009.07.007.
[22] X. Gonze, F. Jollet, F. Abreu Araujo, D. Adams, B. Amadon, T. Applencourt, C. Audouze, J.-M. Beuken, J. Bieder, A. Bokhanchuk, E. Bousquet, F. Bruneval, D. Caliste, M. Cote, F. Dahm, F. Da Pieve, M. Delaveau, M. Di Gennaro, B. Dorado, C. Espejo, G. Geneste, L. Genovese, A. Gerossier, M. Giantomassi, Y. Gillet, D.R. Hamann, L. He, G. Jomard, J. Laflamme Janssen, S. Le Roux, A. Levitt, A. Lherbier, F. Liu, I. Lukacevic, A. Martin, C. Martins, M.J.T. Oliveira, S. Ponce, Y. Pouillon, T. Rangel, G.-M. Rignanese, A.H. Romero, B. Rousseau, O. Rubel, A.A. Shukri, M. Stankovski, M. Torrent, M.J. Van Setten, B. Van Troeye, M.J. Verstraete, D. Waroquier, J. Wiktor, B. Xu, A. Zhou, J.W. Zwanziger, Comput. Phys. Commun. 205 (2016) 106. https://doi.org/10.1016/j.cpc.2016.04.003.
[23] J.P. Perdew, A. Ruzsinszky, G. Csonka, O. Vydrov, G. Scuseria, L. Constantin, X. Zhou, K. Burke, Phys. Rev. Lett. 100 (2008) 136406. https://doi.org/10.1103/PhysRevLett.100.136406.
[24] M.A.L. Marques, M.J.T. Oliveira, T. Burnus, Comput. Phys. Commun. 183 (2012) 2272. https://doi.org/10.1016/j.cpc.2012.05.007.
[25] D.R. Hamann, Phys. Rev. B 88 (2013), 085117, https://doi.org/10.1103/PhysRevB.88.085117.
[26] J.P. Perdew, Y. Wang, Phys. Rev. B 45 (1992) 13244. https://doi.org/10.1103/PhysRevB.45.13244.
[27] X. Gonze, C. Lee, Phys. Rev. B 55 (1997) 10355. https://doi.org/10.1103/PhysRevB.55.10355.
[28] H.T. Stokes, D.M. Hatch, J. Appl. Crystallogr. 38 (2005) 237–238. http://stokes.byu.edu/iso/findsym.php.
[29] D. Orobengoa, C. Capillas, M.I. Aroyo, J.M. Perez-Mato, J. Appl. Crystallogr. A 42 (2009) 820–833. http://www.cryst.ehu.es/cryst/amplimodes.html.
[30] M. Noh, S. Choi, D. Lee, M. Cho, C. Jeon, Y. Lee, New Physics: Sae Mulli 63 (No. 8) (2013) 939–944. https://doi.org/10.3938/NPSM.63.939.
[31] Ph Ghosez, J.-P. Michenaud, X. Gonze, Phys. Rev. B 58 (1998) 6224. https://doi.org/10.1103/PhysRevB.58.6224.
[32] H. Salehi, H. Tolabinejad, Optic Photon. J. 1 (2011) 75–80. https://doi.org/10.4236/opj.2011.12012.
[33] R.I. Eglitis, A.I. Popov, J. Saudi Chem. Soc. 22 (2018) 459. https://doi.org/10.1016/j.jscs.2017.05.011.
[34] R.I. Eglitis, M. Rohlfing, J. Phys. Condens. Matter 22 (2010) 415901. https://doi.org/10.1088/0953-8984/22/41/415901.
[35] A.M. Glazer, Acta Crystallogr. B 28 (1972) 3384. https://doi.org/10.1107/S0567740872007976.
[36] C.J. Howard, H.T. Stokes, Acta Crystallogr. Sect. B Struct. Sci. 54 (1998) 782, 58, 565 (2002), https://doi.org/10.1107/S0108768198004200.
[37] N.A. Benedek, A.T. Mulder, C.J. Fennie, J. Solid State Chem. 195 (2012) 11. https://doi.org/10.1016/j.jssc.2012.04.012.
[38] S. Amisi, University of Liege, Belgium, 2013. Ph.D. thesis, http://hdl.handle.net/2268/158512.
[39] D. Cherrad, D. Maouche, Physica B 405 (2010) 3862–3868. https://doi.org/10.1016/j.physb.2010.06.018.
[40] http://www.me.utexas.edu/\~benedekgroup/ToleranceFactor_Calculator/\#home.
[41] D. Vanderbilt, W. Zhong, First-principles theory of structural phase transitions for perovskites: competing instabilities, Ferroelectrics 206 (1998) 181–204.
[42] https://www.ulg.ac.be/cms/c_3826073/fr/nic4. http://www.ceci-hpc.be/.